



# An Easily Assembled Electromagnetic-Triboelectric Hybrid Nanogenerator Driven by Magnetic Coupling for Fluid Energy Harvesting and Self-Powered Flow Monitoring in a Smart Home/City

Yiming Zhong, Haibo Zhao, Yuanchao Guo, Pinshu Rui, Shiwei Shi, Wen Zhang, Yanlin Liao, Peihong Wang,\* and Zhong Lin Wang\*

Harvesting wind energy and water flow energy from the living environment to efficiently and conveniently power many small electric devices at home is becoming increasingly important for the development of the smart home system. Triboelectric nanogenerators (TENGs) are considered to be one of the most effective devices to harness various types of mechanical energy. Here, an easily assembled electromagnetic-triboelectric hybrid nanogenerator (EANG) driven by magnetic coupling is reported. The introduction of magnetic coupling makes it easy to package, maintain, and assemble a nanogenerator (NG), so its performance is very stable regardless of environmental variations. A sliding freestanding mode TENG and a rotary electromagnetic generator (EMG) are integrated to improve their output and broaden the frequency range of external energy. It is shown that the EANG can be conveniently integrated with a wind cup or water turbine and harvest fluid energy to power small electronic devices, such as a humidity sensor and temperature sensor. Moreover, a NG can be used as a self-powered flow sensor to monitor the flow rate of outdoor wind and tap water. These results can be used to help solve practical problems regarding energy supplying and sensing in a smart home, smart building, and smart city.

with smart devices, is driven by reliable power. With the continuous development of microelectromechanical systems and the Internet of Things (IoT), many small electronic devices, which require a sustainable, portable, distributed, wireless, and even implantable power source, are increasingly widely used in daily life and industrial monitoring environments.<sup>[1]</sup> However, traditional power supply solutions, which include electric cables and batteries, cannot fully satisfy their special demands.<sup>[2]</sup> Fortunately, mechanical energy, which is widely present in the environment, such as via wind and water flow, contains a large amount of easily accessible energy.<sup>[3]</sup>

Regarding mechanical energy harvesting techniques, until now, four main energy conversion mechanisms are used: electromagnetic,<sup>[4]</sup> piezoelectric,<sup>[5]</sup> electrostatic,<sup>[6]</sup> and triboelectric.<sup>[7]</sup> In particular, triboelectric nanogenerators (TENGs), which were first described by Wang and

coworkers in 2012<sup>[8]</sup> and are based on the triboelectrification effect and electrostatic induction, are becoming the most important devices since they have many advantages, such as simple fabrication, light weight, low cost, high output voltage, and high durability, especially for human-related activities. Recently,

## 1. Introduction

Today's society, which depends on convenient communication via smartphones and the internet as well as automobiles, modern medical devices and almost everything associated

Y. Zhong, H. Zhao, Y. Guo, P. Rui, Dr. S. Shi, W. Zhang,  
Dr. Y. Liao, Prof. P. Wang  
School of Physics and Materials Science  
Energy Materials and Devices Key Lab of Anhui Province  
for Photoelectric Conversion  
Anhui University  
Hefei 230601, Anhui, P. R. China  
E-mail: wangpeihong2002@ahu.edu.cn

Prof. P. Wang  
Key Laboratory of Structure and Functional Regulation of Hybrid Materials  
Anhui University  
Ministry of Education  
Hefei 230601, Anhui, P. R. China

 The ORCID identification number(s) for the author(s) of this article can be found under <https://doi.org/10.1002/admt.201900741>.

DOI: 10.1002/admt.201900741

Prof. Z. L. Wang  
Beijing Institute of Nanoenergy and Nanosystems  
Chinese Academy of Sciences  
Beijing 100083, P. R. China  
E-mail: zhong.wang@mse.gatech.edu

Prof. Z. L. Wang  
School of Materials Science and Engineering  
Georgia Institute of Technology  
Atlanta, GA 30332-0245, USA

the fundamental mechanism of triboelectrification has been systematically studied by Wang,<sup>[9]</sup> and many studies have shown that TENGs can be used to harvest energy from a variety of sources, including wind, water flow, and other mechanical motions.<sup>[10]</sup> Xie et al. reported a rotary TENG based on a wind cup structure to harvest wind energy and measure wind speed in 2013.<sup>[11]</sup> By using similar structures, Zhang et al. presented a rotating-disk-based hybridized electromagnetic-triboelectric NG to sustainably power wireless traffic volume sensors by harvesting wind energy in 2016,<sup>[12]</sup> and Wang et al. proposed an anemometer triboelectric nanogenerator for a highly efficient wind energy harvesting and self-powered wind speed sensor system in 2018.<sup>[13]</sup> To harvest both wind energy and water flow energy, Zhu et al. reported a two-dimensional planar-structured and radial-arrayed rotary TENG in 2014,<sup>[14]</sup> Guo et al. presented a water-proof triboelectric-electromagnetic hybrid generator in 2016<sup>[15]</sup> and Xi et al. proposed a multifunctional TENG in 2017.<sup>[16]</sup> Although these NGs perform well, some of them can only harvest energy from a single source. Meanwhile, it is difficult to encapsulate, maintain and reinstall some NGs<sup>[11,12,14–16]</sup> because the driving and power-generating parts are fixed. These disadvantages limit real application of these NGs.

This work presents an easily assembled electromagnetic-triboelectric nanogenerator (EANG) driven by magnetic coupling to harvest fluid energy. We use the noncontact magnetic attractive force generated by the magnetic coupling to drive the NG.

This design simplifies the full packaging of the NG. The NG can be easily unloaded, maintained and reinstalled because there is no physical connection between the magnetic driver and the NG. Moreover, a sliding freestanding TENG and a rotary disc electromagnetic generator (EMG) are hybridized to improve the performance of the NG.<sup>[17]</sup> The experimental results and the demonstration show that the hybrid NG has a higher output than a single TENG or a single EMG. Meanwhile, the NG can conveniently scavenge fluid energy, including wind and water energy, and power many electric devices, such as light emitting diodes (LEDs), humidity sensors and temperature sensors. In addition, the NG can be used as a self-powered flow sensor with good accuracy compared to commercial flow meters. Therefore, this work is significant for both the packaging of a hybrid NG and its practical applications, especially regarding water flow energy harvesting and flow monitoring in smart home systems.

## 2. Results and Discussion

### 2.1. Design and Working Principle

The structural design of the hybrid nanogenerator driven by magnetic coupling is shown in **Figure 1a**. The hybrid NG mainly consists of a cylindrical stator and a cylindrical rotator. The rotator is a small cylinder with two covers (Figure 1c).

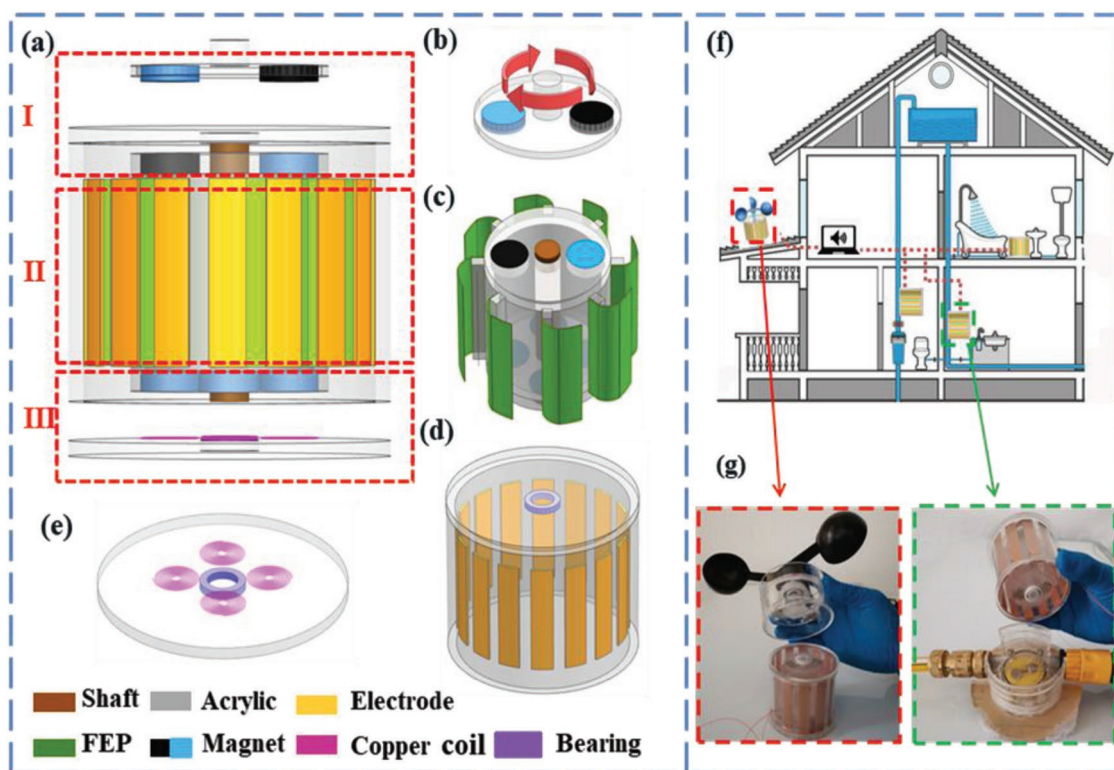


**Figure 1.** Structural design and application of the hybrid nanogenerator in a smart home. a) Schematic diagram of the designed hybrid nanogenerator, including a magnetic coupling (I), a sliding freestanding mode TENG (II) and an EMG (III). b) Driving part of the magnetic coupling. c) Rotator of the NG (i.e., the follower of the magnetic coupling). d) Stator of the NG with the upper cover. e) Lower cover of the stator with four coils and one bearing. f) Schematic diagram of the practical application of the EANG in a smart home. g) Optical images of the EANG with a wind cup or water turbine to harvest outdoor wind energy and water flow energy in a water pipe.

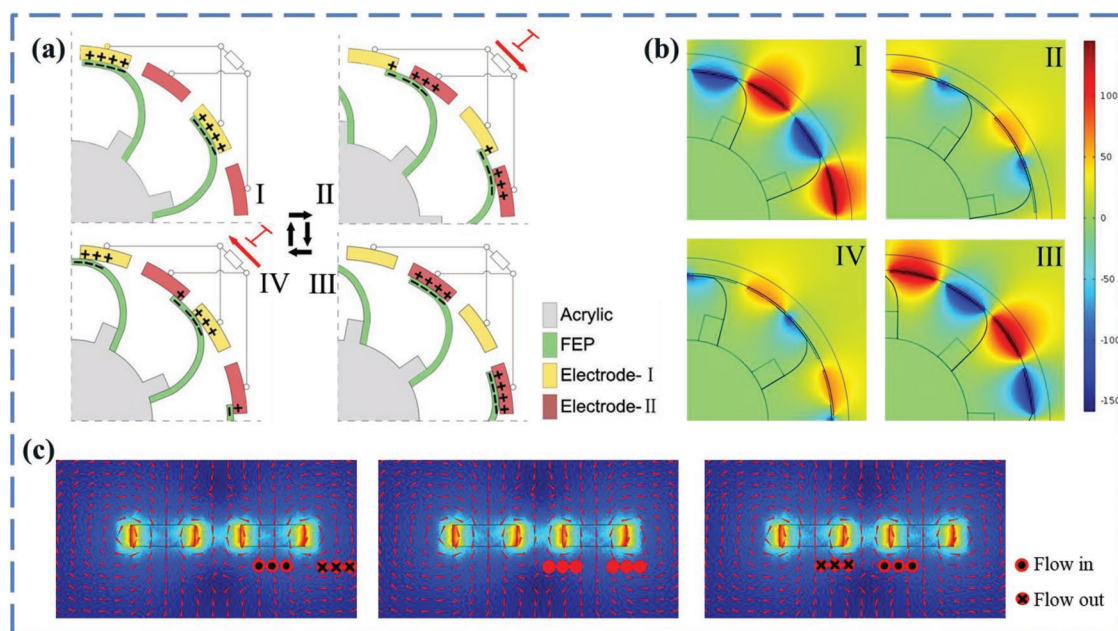


**Figure 2.** Schematic diagrams of the working principle of the hybrid nanogenerator. a) Scheme of the working mechanism of the TENG. b) Numerical calculations of the potential distribution of the electrodes of the TENG. c) Finite element simulation results of the working principle of the EMG.

Several pieces of fluorinated ethylene propylene (FEP) films are attached on the outer surface of the small cylinder. Two magnets with different magnetic pole directions are embedded in the upper cover of the rotator. Four magnets with identical magnetic pole directions are embedded in the lower cover of the rotator. The stator is composed of a large cylinder and two covers (Figure 1d). Several pieces of copper (Cu) foils are attached to the inside surface of the stator to form two groups of electrodes. Two bearings are embedded in the inner center of the upper and lower covers of the stator. Four Cu coils are fixed on the inner surface of the lower cover of the stator (Figure 1e). A shaft goes through the rotator and connects the two bearings. Moreover, the shaft and the rotator are glued together. A disk (Figure 1b) in which two magnets are embedded is normally called a driver in a magnetic coupling. The driver and the rotator comprise a magnetic coupling. When the external torque drives the driver to rotate, the rotator spins under the magnetic coupling force. Therefore, the rotating FEP film blades and the fixed Cu electrodes form a sliding freestanding mode TENG (Figure 1aII). Meanwhile, the four rotating magnets on the lower cover of the rotator and the four coils on the lower cover of the stator comprise an EMG (Figure 1aIII).

The presented hybrid nanogenerator driven by magnetic coupling has several clear features. First, the magnetic coupling can transmit the external torque from the driver to the rotator through space with no physical contact.<sup>[18]</sup> This feature makes the structure simpler than traditional NGs, which have a shaft connecting the driver and the rotator.<sup>[15,16,19]</sup> Second, the EANG is very easy to unload, maintain and reassemble since there is no mechanical connection between the driver and the rotator. Therefore, the hybrid NG can be easily connected with various external torques from wind and water, as shown in Figure 1g, whereas many traditional hybrid NGs can only harvest one type of energy.<sup>[11–13,20]</sup> Third, the EANG can easily be fully

encapsulated to become waterproof, which would stabilize its output performance and make it adaptable to various harsh environments. Fourth, the soft contact between the blades and the electrodes has less friction than the traditional solid–solid contact, which has been proven by our group.<sup>[21]</sup> As a result, the EANG can harvest very weak rotation energy, such as weak wind and slow water flow. Therefore, the EANG presented in this work has many real applications, particularly in smart housing (Figure 1f).

The working principle of the hybrid NG is shown in Figure 2. Regarding the TENG, Figure 2a concisely shows how the sliding freestanding triboelectrification works in four steps. In the initial state (Step I), the FEP film blades contact Electrode I. The electrons are transferred from Electrode I to the FEP film because of the contact triboelectrification effect.<sup>[22]</sup> The positive charges on the electrodes are equal to the negative charges on the surface of the FEP film. When the rotator starts rotating under external stimulation (Step II), the electrons in Electrode II will flow into Electrode I through an outside circuit to maintain the electrostatic equilibrium between the two electrodes. Thus, a current from Electrode I to Electrode II is generated. When the films totally overlap with Electrode II (Step III), all positive charges are driven to Electrode I. As the relative rotation continues, the FEP film begins to leave Electrode II and aligns with Electrode I again. The reverse current will flow through the external circuit (Step IV). The numerical calculations of the electrical potential distribution across the electrodes of the TENG are shown in Figure 2b, which correspond with the four steps shown in Figure 2a. It is clearly shown that the potential difference between Electrodes I and II results in the flow of electrons in the external circuit.

The operating principle of the EMG is Faraday's induction law and is shown in Figure 2c. When the coil rotates to align with the magnet (Figure 2cI), the increase in the magnetic

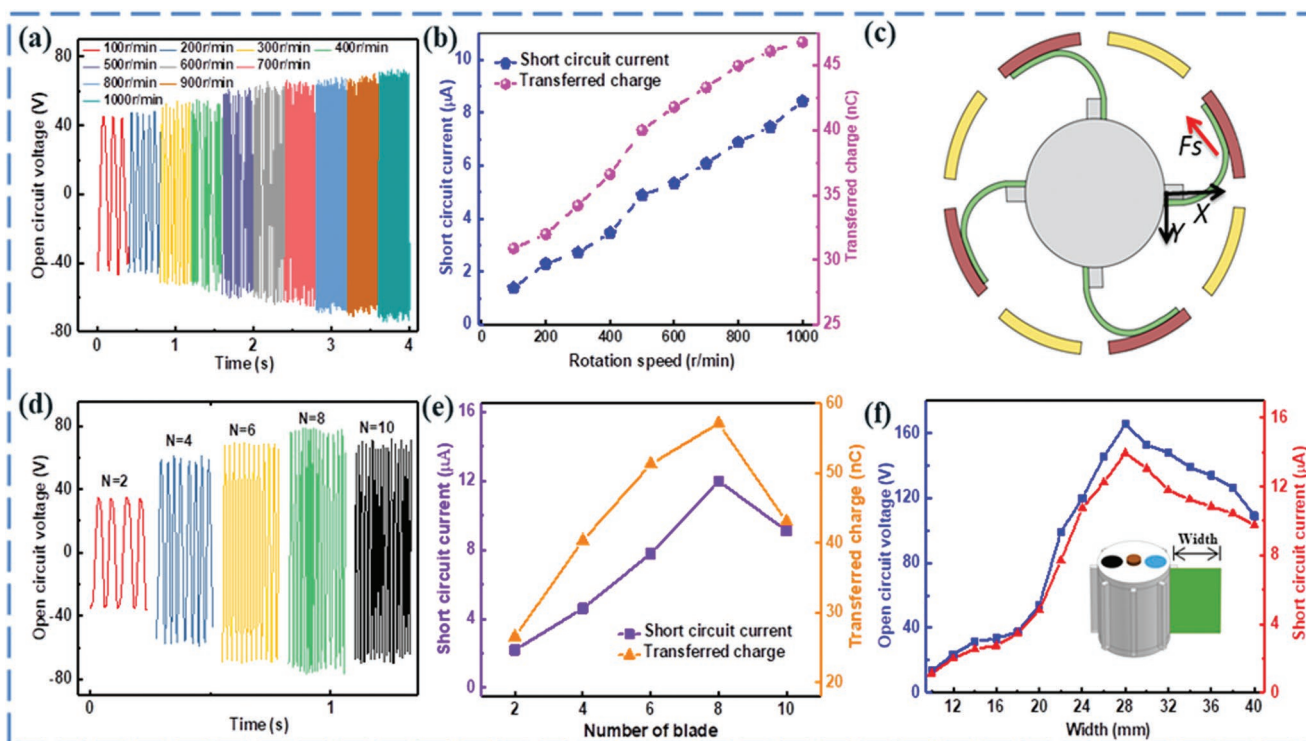


**Figure 3.** Output performance of the TENG. a) Open-circuit voltage of the TENG versus time under different rotation speeds, b) short-circuit current and the transferred charge of the TENG with different rotation speeds, c) schematic of the blade under the supporting force from the stator, d) open-circuit voltage of the TENG versus time with different numbers of film blades, e) short-circuit current and the transferred charge of the TENG versus the number of FEP film blades, and f) open-circuit voltage and short-circuit current of the TENG with different widths of the FEP film.

flux linkage crossing the coil induces a current in the coil. When the coil is aligned with the magnet (Figure 2cII), the magnetic flux linkage reaches its maximum and the induced current is zero. Subsequently, an induced current with the opposite direction is generated in the coil with the decrease in magnetic flux linkage, as shown in Figure 2cIII. This process repeats, and the induced current is continuously generated in the coil.

## 2.2. Output Characterization

To systematically characterize the ability of the EANG to harvest rotation energy, it is driven by an electronic motor, and the effect of the rotation speed on the output performance is studied. The  $V_{oc}$ ,  $I_{sc}$ , and  $Q_{sc}$  of the TENG versus time are shown in Figure 3a and Figure S1a,b (Supporting Information), respectively. As shown in Figure 3a,  $V_{oc}$  increases from 89 to 144 V when the rotating speed increases from 100 to 1000  $r\ min^{-1}$ . In addition, the  $I_{sc}$  and  $Q_{sc}$  of the TENG have the same linear increasing trend: they increase from 2.2 to 8.3  $\mu A$  and 32 to 45 nC, respectively (Figure 3b). Our TENG has clearly different results from a traditional rotary TENG, in which only the short-circuit current increases with the rotation speed.<sup>[14,16]</sup> In the design of our TENG shown in Figure 3c, the film blade is soft and flexible, so the elastic force is very small when it deforms under an external force. The elastic force is not sufficient to provide centripetal force to the film blade when the rotation is

too fast. As a result, more parts of the blade contact the stator, so the supporting force ( $F_s$ ) from the stator can supply more centripetal force to the blade. Then, the contact area increases, and  $V_{oc}$  and  $Q_{sc}$  increase accordingly when the rotation speed increases.<sup>[21]</sup> Therefore, the design of the soft contact in the TENG helps to increase the transferred charge and output power. Second, the number of FEP film blades is optimized. In this experiment, the number of film blades is defined as “N,” so the number of electrodes is “2N.” We maintain a constant total area of the Cu electrode and change the value of N. As shown in Figure 3d,e, and Figure S1c,d (Supporting Information), when the number of FEP blades varies from 2 to 10, the open-circuit voltage, short-circuit current, and transferred charge increase until N is equal to 8 and subsequently decrease. Their maximum values are 157 V, 11.5  $\mu A$ , and 64 nC, respectively. When N is equal to 10, the FEP blade will contact two adjacent electrodes at any time (Figure S2, Supporting Information) and the transferred charge decreases, which results in a decrease in performance of the TENG. Therefore, eight FEP blades should be used as the standard for all devices. Third, the width of the FEP film blade is an important issue in structural optimization, and its effect on the performance of the TENG is studied. As shown in Figure 3f, the peak values of the  $I_{sc}$  and  $V_{oc}$  of the TENG increase until the width reaches 28 mm and subsequently decrease when the width of the film continues to increase. An excessively wide film blade allows it to always simultaneously connect two electrodes, and the performance of the TENG decreases. As a result, the width of the FEP film

blade is set as 28 mm in the optimized structure of the TENG in the following experiment.

As is known, environmental humidity strongly affects the electrical performance of the TENG, so maintaining a stable output of the TENG is a problem that must be solved.<sup>[23]</sup> The rigid connection between the driving part and the power generation part of the TENG makes full encapsulation difficult in many previous works,<sup>[11,14,16]</sup> which limits its real application. However, for our designed EANG, the package is very easy and simple since the drive part do not directly connect to the rotator. The detailed encapsulation process is given in Experimental Section below and a movie describing the assembling and encapsulating process is presented as Movie S1 in the Supporting Information. The  $V_{oc}$ ,  $I_{sc}$ , and  $Q_{sc}$  versus time of the TENG encapsulated in normal air or in glove box are shown in Figure 4a–c, respectively, and they are compared in Figure S3a in the Supporting Information. The comparison results show that the  $V_{oc}$ ,  $I_{sc}$ , and  $Q_{sc}$  of the TENG encapsulated in glove box increase by 26.2%, 9.3%, and 8.6%, respectively. Furthermore,

its output performance under various rotation speeds was measured. Figure 4d indicates that the  $V_{oc}$ ,  $I_{sc}$ , and  $Q_{sc}$  of the sealed TENG in a glove box are 270 V, 27.7  $\mu$ A, and 86.1 nC, respectively, when the rotation speed is 2000  $r\ min^{-1}$ . The robustness of the TENG was investigated at a rotation speed of 500  $r\ min^{-1}$ , and the result is shown in Figure 4e. The open-circuit voltage of the TENG had almost no change after 50 000 cycles of operation, which shows that the TENG has good reliability and durability. The output performance of the EMG is shown in Figure 4f. The  $V_{oc}$  and  $I_{sc}$  of the EMG linearly increase with the rotation speed, which is consistent with Faraday's induction law. To investigate the optimal output conditions of the TENG and EMG, their load voltage and load power under different resistances were measured and are shown in Figure 4g,h. As shown in Figure 4g, the maximum load voltage of the TENG can reach  $\approx 200$  V at 100 M $\Omega$ . The maximal load power is 1.05 mW when the load resistance is  $\approx 4$  M $\Omega$ . Figure 4h indicates that the maximum load voltage of the EMG is  $\approx 5$  V at 4 k $\Omega$  and the maximal load power is 58.3 mW at a matched load resistance of 20  $\Omega$ .

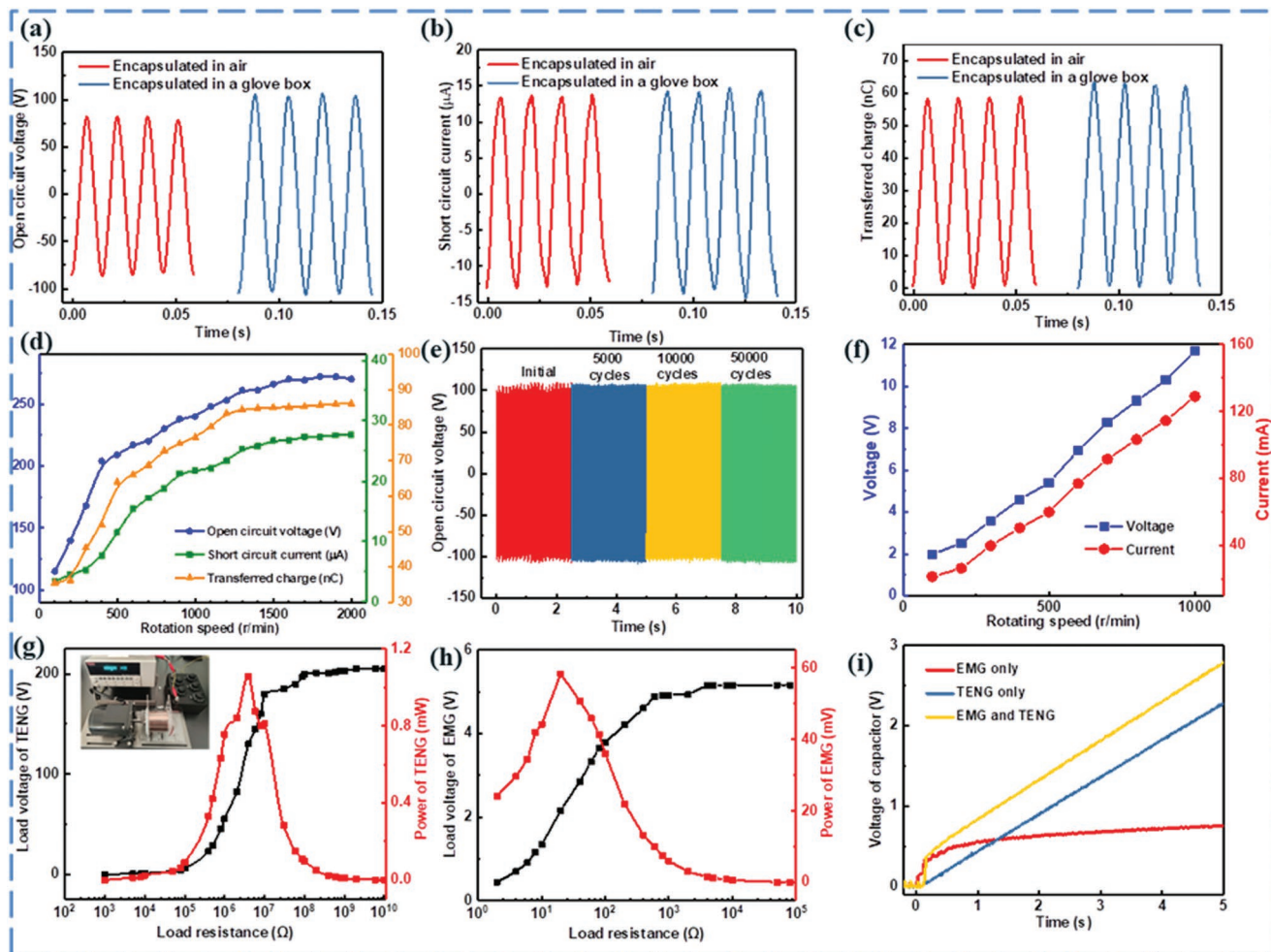


**Figure 4.** Experimental results of the hybrid NG. Comparison of the a) open-circuit voltage, b) short-circuit current, and c) transferred charge of the TENG encapsulated in normal air or in a glove box with stable humidity/temperature. d) Output performance of the sealed TENG with different rotating speeds. e) Comparison of the open-circuit voltage of the TENG after 5000, 10 000, and 50 000 cycles. f) Output voltage and current of the EMG versus the rotation speed. Output voltage and power under different external load resistances of the g) TENG and h) EMG under a rotation velocity of 500  $r\ min^{-1}$ . i) Charging curves of the EMG, TENG, and hybrid NG when the capacity is 22  $\mu$ F and the rotation speed is 500  $r\ min^{-1}$ .

To investigate the charging capability of the EANG, a capacitor of 22  $\mu\text{F}$  was used in this experiment. As shown in Figure 4i, the individual EMG has a fast charging speed, but the voltage on the capacitor reaches a saturation 0.7 V in 1 s. On the contrary, the individual TENG has a slow charging speed, but the voltage on the capacitor continues to increase. When the charging time is 5 s, the voltages of the capacitor charged by the EANG, individual TENG and individual EMG are 2.8, 2.28, and 0.75 V, respectively, which shows that the EANG has the best charging performance. Moreover, the effect of the rotation speed on the voltage on the capacitor and the charging curve of different capacitors were measured and are shown in Figure S3b,c in the Supporting Information. A high rotation speed and a small capacitor help to obtain a high voltage on the capacitor in a short amount of time.

### 2.3. Demonstrations

First, 61 green and 61 red LEDs arranged into “AHU” were connected with the TENG and EMG (Figure 5a) to demonstrate the capability of this hybrid NG to act as a direct power

source. As shown in Movie S2 in the Supporting Information, the green LEDs are lit by the TENG when the rotation speed reaches  $\approx 300 \text{ r min}^{-1}$ . However, the red LEDs driven by the EMG begin to glow when the rotating speed is  $\approx 700 \text{ r min}^{-1}$ . This lighting sequence proves the different capabilities of the EMG and TENG to harvest rotating energy and the necessity of combining them.<sup>[24]</sup> As shown in Figure S4a in the Supporting Information, 254 LEDs can be lit by the hybrid NG when the rotating speed is  $500 \text{ r min}^{-1}$ .

Second, the capability of the EANG to harvest fluid energy and monitor the flow rate in a real environment was investigated in detail, and the basic functional schematic is shown in Figure 5d. As shown in Figure 5b, a water turbine integrated into a water pipe was used to drive the NG. A commercial water flowmeter (Lungbor-K24) is used to measure the flow rate in real time. The rotation speed ( $V_{\text{rotation}}$ ) of TENG could be calculated by using the following equation:  $V_{\text{rotation}} = f_{\text{voc}} \cdot 60/N$ , where  $f_{\text{voc}}$  is the frequency of the  $V_{\text{oc}}$  of the TENG and  $N$  is the number of the blades of the TENG. In the optimized NG used in the demonstration,  $N = 8$ . As shown in Figure 5c, the rotating speed linearly increases with the flow rate. Meanwhile, the output voltage of the TENG increases from 195 to 260 V when

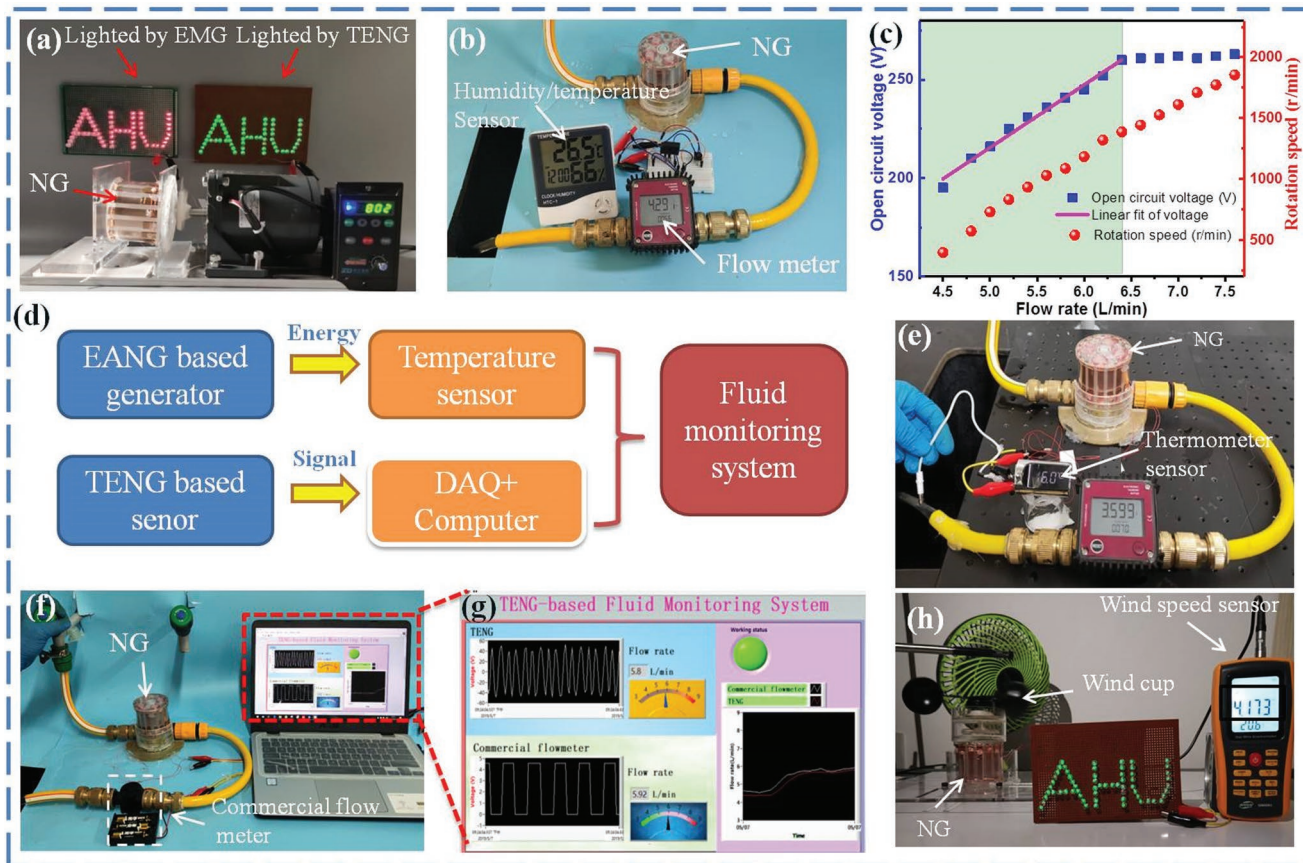


**Figure 5.** Demonstrations of the EANG for various applications. a) Photograph of red and green LEDs lit by the individual EMG and individual TENG driven by a motor. b) EANG to harvest ting water flow energy to power a humidity sensor. c) Relationship between the open-circuit voltage of the TENG, rotating speed, and flow rate. d) System diagram of a self-powered fluid monitoring system. e) Photograph of a thermometer sensor successfully driven by the EANG to detect the water temperature. f) Photograph of the measurement platform to compare the detection ability the EANG and the commercial flow meter. g) Real-time fluid monitoring interface programmed by LabVIEW software. h) Photograph of the NG harvesting wind energy and lighting LED arrays at a wind speed of  $4 \text{ m s}^{-1}$ .

the flow rate increases from 4.5 to 6.4 L·min<sup>-1</sup>, and it remains stable with further increase in flow rate. The lack of change in output voltage under a high flow rate may be due to the constant contact area between the film blade and the electrode, which cannot further increase under high rotation speeds, and the open circuit voltage remains stable. Thus, the sensitivity of the TENG in the linear region is ≈31.9 V L<sup>-1</sup>·min<sup>-1</sup>. In this experiment, the water turbine has many small blades as shown in Figure S5 in the Supporting Information, which results in high rotation speed under small flow rate. In future, we will use 3D printing technique to fabricate a water turbine with fewer blades and as a result the effective measuring range of flow rate will be enlarged. As shown in Figure 5b and Movie S3 in the Supporting Information, a humidity/temperature sensor is successfully activated by the hybrid NG when the flow rate is ≈6.0 L min<sup>-1</sup>. The corresponding circuit is shown in Figure S4b in the Supporting Information. Moreover, a thermometer with a LED display (BD-LS-01) can be powered by the hybrid NG to monitor the water temperature in the water pipe in real time, as shown in Figure 5e. Movie S4 in the Supporting Information shows that the flow rate increases to 6.7 L min<sup>-1</sup> in 6 s and the thermometer begins to work at an initial temperature of 25 °C. When the sensor probe is inserted into the water flow, the thermometer displays a water temperature of 22.5 °C.

Third, the TENG can be used as a self-powered flow sensor to detect the flow rate of water using a fluid monitoring system based on the LabVIEW software, as shown in Figure S4c in the Supporting Information. Figure S4d and Movie S4 in the Supporting Information indicate that the flow rate and flow capacity are displayed in real time in the monitoring system. Furthermore, the TENG-based flow sensor is compared with a commercial flow meter to verify its accuracy. As shown in Figure 5f,g and Movie S5 (Supporting Information), the commercial flow meter (YFS201) requires a DC power of 4.5 V to generate a square-wave voltage signal;<sup>[25]</sup> however, the TENG can directly generate a sine-wave voltage signal with no power. The flow meter can generate 450 square-wave voltage signals when 1 L water flows through the flow meter. Thus, the flow rate ( $X$ ) of the flow meter could be calculated by using the following equation  $X = 60/(450 \cdot T)$ , where  $T$  is the period time of the square-wave signal.<sup>[25]</sup> The flow rate from the TENG can be calculated from the relationship between the rotation speed and the flow rate shown in Figure 5c. The above calculation can be realized by the fluid monitoring system which is programmed by us. The monitoring system can display the real-time value of the flow rate and the curve of the flow rate versus time, as shown in Figure 5g. The flow rates measured by the TENG-based flow meter and commercial flow meter are 5.8 and 5.92 L min<sup>-1</sup>, respectively. The error is only 2.0%.

Finally, the capability of the EANG to harvest ambient wind energy is investigated. In this experiment, an electric fan was used to supply wind to drive a wind cup. The wind cup with two magnets and the rotator of the hybrid NG comprise a magnetic coupling, and the hybrid NG can be driven by the wind cup. A commercial hot-wire anemometer was used to detect the wind speed. As shown in Figure 5h and Movie S6 in the Supporting Information, the LEDs arranged in the shape of "AHU" were lighted by the hybrid NG when the speed was 4.2 m s<sup>-1</sup>. Moreover, the relationship between the  $V_{oc}$  of the TENG and the wind

speed was measured and is shown in Figure S6 in the Supporting Information. The results clearly indicate that  $V_{oc}$  is almost linear with the wind speed and that the sensitivity is 6.4 V m s<sup>-1</sup>. For this hybrid NG, the lack of a physical connection between the driver and the rotator helps to decrease the required torque when the rotator starts to spin. Therefore, the TENG-based wind speed sensor has a lower threshold of wind speed of ≈3 m s<sup>-1</sup>. This threshold is smaller than that of previous TENG-based wind speed sensors from us and other researchers.<sup>[16,21,26]</sup>

All of the above demonstrations show that the presented EANG is easily assembled, easy to maintain, fully waterproof and multifunctional. The presented EANG has numerous applications, especially in harvesting water flow energy and functioning as a self-powered flow sensor in smart buildings and industry in the future.

### 3. Conclusions

In summary, an easily assembled electromagnetic-triboelectric hybrid nanogenerator driven by magnetic coupling to harvest fluid energy is presented in this work. The introduction of a magnetic coupling makes the encapsulation, installation, and maintenance of the hybrid NG much easier. Meanwhile, the friction that prevents the rotator from rotating is decreased by the magnetic coupling and the soft contact between the triboelectric film and the electrode. The combination of the EMG and TENG increases the output performance of the hybrid NG. The experimental results show that after optimization and full encapsulation, the TENG has a  $V_{oc}$  of 270 V,  $I_{sc}$  of 27.7 μA, and  $Q_{sc}$  of 86.1 nC when the rotation speed is 2000 r min<sup>-1</sup>. At a rotating speed of 500 r min<sup>-1</sup>, the  $V_{oc}$  and the maximal load power of the TENG are 48 V and 1.05 mW, respectively, under a load resistance of 4 MΩ and the  $V_{oc}$  and the maximal output of the EMG are 4.8 V and 58.3 mW, respectively, under a load resistance of 20 Ω. The demonstration indicates that this EANG can be easily used to harvest fluid energy, including wind energy and water flow energy, and to power small electric devices, such as LEDs, a humidity sensor, and a thermometer. Moreover, the results show that the hybrid NG performs well as a self-powered flow sensor to monitor the water flow rate and wind speed. Therefore, the EANG presented in this work has numerous applications in smart housing/building/factories, real industry, and other fields in the future.

### 4. Experimental Section

*Fabrication of the EANG:* The EANG mainly consists of three parts: a rotator, a stator, and an external connection part. The rotator was made of an acrylic inner cylinder (diameter: 40 mm; height: 45 mm) with upper and bottom covers (thickness: 3 mm). On the outer surface of the inner cylinder, eight acrylic strips (length: 40 mm; width: 4 mm; height: 3 mm) were evenly attached and eight FEP films (thickness: 50 μm), which were cut into a specific size, were taped one side of the strip. Then, two NdFeB magnets (diameter: 12 mm; height: 4 mm) with opposite polarities were evenly arranged and embedded in the upper cover as a part of the magnetic drive section. Four identical magnets with the same polarity were embedded in the bottom cover as the permanent array of the disc EMG. For the stator, a larger acrylic cylinder (diameter: 65 mm; height: 55 mm) was the main outer frame. Two acrylic sheets (diameter:

65 mm; thickness: 3 mm) were drilled with half-through holes, while plastic bearings (JCS POM688) were embedded in the holes to form the upper and lower covers of the outer cylinder. Four coils (inner diameter: 12 mm; outer diameter: 19 mm; turns: 480; height: 2 mm) were mounted to the bottom cover. On the inside wall of the outer cylinder, sixteen copper foil (length: 40 mm; width: 3.75 mm; thickness: 60  $\mu\text{m}$ ) were evenly arranged and attached with glue, and the total effective area was maintained at 24  $\text{cm}^2$ . An aluminum central shaft was fixed with the rotor and connected with the bearings of the stator. Then, the hybrid nanogenerator was first assembled and then it was encapsulate by using the glue to fix the top and bottom cover on the outer cylinder. As a result, the interior and exterior of the NG were isolated. In order to compare the TENG's output under different conditions, the NG was encapsulated in normal air (temperature:  $\approx 20^\circ\text{C}$ , humidity:  $\approx 30\%$ ) or in a glove box (temperature:  $\approx 20^\circ\text{C}$ , humidity:  $\approx 10\%$ ). In order to prove that the NG had good sealing property, the encapsulated NG was put into the water and it was found that no air bubbles appeared. The corresponding movie is supplied as Movie S7 in the Supporting Information. Finally, one side of the external connection part was an acrylic disk, which was embedded in two opposite magnets, and the other side connects with various external rotating mechanisms.

**Electrical Measurement:** The output electrical performance of the EANG was measured by an electrometer (Keithley, 6514). A data acquisition card (NI, USB 6211) and the LabVIEW software platform were used to acquire and analyze the data. A commercial motor (ZD-5IK40W) was used to make the device rotate.

## Supporting Information

Supporting Information is available from the Wiley Online Library or from the author.

## Acknowledgements

This work was supported by the National Natural Science Foundation of China (61671017), Excellent Youth Talent Support Program in Colleges and Universities of Anhui Province in China (gxyqZD2018004), Provincial Natural Science Foundation of Anhui Higher Education Institution of China (KJ2016A787), and Anhui Provincial Natural Science Foundation of China (1508085ME72).

## Conflict of Interest

The authors declare no conflict of interest.

## Keywords

fluid energy, hybrid nanogenerators, magnetic coupling, self-powered flow sensors, triboelectric nanogenerators

Received: August 28, 2019

Revised: October 11, 2019

Published online:

- [1] a) J. Iannacci, *Sens. Actuators, A* **2018**, 272, 187; b) J. Ma, Y. Jie, J. Bian, T. Li, X. Cao, N. Wang, *Nano Energy* **2017**, 39, 192; c) M. Talal, A. A. Zaidan, B. B. Zaidan, A. S. Albahri, A. H. Alamoody, O. S. Albahri, M. A. Alsalem, C. K. Lim, K. L. Tan, W. L. Shir, K. I. Mohammed, *J. Med. Syst.* **2019**, 43, 42; d) F. Wang, L. Hu,

- J. Hu, J. Zhou, K. Zhao, *IETE Tech. Rev.* **2017**, 34, 122; e) B. Zhou, W. T. Li, K. W. Chan, Y. J. Cao, Y. H. Kuang, X. Liu, X. Wang, *Renewable Sustainable Energy Rev.* **2016**, 61, 30.  
 [2] a) M. Saliba, *Science* **2018**, 359, 388; b) P. Maharjan, R. M. Toyabur, J. Y. Park, *Nano Energy* **2018**, 46, 383; c) M. Salauddin, R. M. Toyabur, P. Maharjan, J. Y. Park, *Nano Energy* **2018**, 45, 236.  
 [3] a) R. Cao, T. Zhou, B. Wang, Y. Y. Yin, Z. Q. Yuan, C. J. Li, Z. L. Wang, *ACS Nano* **2017**, 11, 8370; b) J. Wang, L. Tang, L. Zhao, Z. Zhang, *Energy* **2019**, 172, 1066; c) M. Xu, T. Zhao, C. Wang, S. L. Zhang, Z. Li, X. Pan, Z. L. Wang, *ACS Nano* **2019**, 13, 1932; d) S. Lee, S.-H. Bae, L. Lin, Y. Yang, C. Park, S.-W. Kim, S. N. Cha, H. Kim, Y. J. Park, Z. L. Wang, *Adv. Funct. Mater.* **2013**, 23, 2445; e) H. Wang, Q. Zhu, Z. Ding, Z. Li, H. Zheng, J. Fu, C. Diao, X. Zhang, J. Tian, Y. Zi, *Nano Energy* **2019**, 57, 616; f) H. Phan, D.-M. Shin, S. H. Jeon, T. Y. Kang, P. Han, G. H. Kim, H. K. Kim, K. Kim, Y.-H. Hwang, S. W. Hong, *Nano Energy* **2017**, 33, 476.  
 [4] a) P. H. Wang, K. Tanaka, S. Sugiyama, X. H. Dai, X. L. Zhao, J. Q. Liu, *Microsyst. Technol.* **2009**, 15, 941; b) K. Fan, Q. Tan, H. Liu, M. Cai, H. Qu, *Smart Mater. Struct.* **2019**, 28, 07LT01.  
 [5] a) K. Tao, H. Yi, L. Tang, J. Wu, P. Wang, N. Wang, L. Hu, Y. Fu, J. Miao, H. Chang, *Surf. Coat. Technol.* **2019**, 359, 289; b) P. Wang, X. Liu, H. Zhao, W. Zhang, X. Zhang, Y. Zhong, Y. Guo, *J. Intell. Mater. Syst. Struct.* **2019**, 30, 1094.  
 [6] a) Y. Suzuki, *IEEJ Trans. Electr. Electron. Eng.* **2011**, 6, 101; b) K. Tao, L. H. Tang, J. Wu, S. W. Lye, H. L. Chang, J. M. Miao, *J. Microelectromech. Syst.* **2018**, 27, 276.  
 [7] a) Z. L. Wang, *Nano Energy* **2018**, 54, 477; b) C. S. Wu, A. C. Wang, W. B. Ding, H. Y. Guo, Z. L. Wang, *Adv. Energy Mater.* **2019**, 9, 25.  
 [8] F.-R. Fan, Z.-Q. Tian, Z. L. Wang, *Nano Energy* **2012**, 1, 328.  
 [9] a) Z. L. Wang, *Mater. Today* **2017**, 20, 74; b) Z. L. Wang, *Nano Energy* **2019**, 58, 669; c) Z. L. Wang, A. C. Wang, *Mater. Today* **2019**, <https://doi.org/10.1016/j.mattod.2019.05.016>; d) C. Xu, Y. Zi, A. C. Wang, H. Zou, Y. Dai, X. He, P. Wang, Y.-C. Wang, P. Feng, D. Li, Z. L. Wang, *Adv. Mater.* **2018**, 30, 1706790.  
 [10] a) Y. C. Lai, Y. C. Hsiao, H. M. Wu, Z. L. Wang, *Adv. Sci.* **2019**, 6, 1801883; b) R. Y. Zhang, M. Hummelgard, J. Ortegren, M. Olsen, H. Andersson, H. Olin, *Nano Energy* **2019**, 57, 279; c) T. Kim, S. Jeon, S. Lone, S. J. Doh, D.-M. Shin, H. K. Kim, Y.-H. Hwang, S. W. Hong, *Nano Energy* **2018**, 54, 209; d) H.-Y. Park, H. K. Kim, Y.-H. Hwang, D.-M. Shin, *J. Korean Phys. Soc.* **2018**, 72, 499; e) J. Chen, B. Chen, K. Han, W. Tang, Z. L. Wang, *Adv. Mater. Technol.* **2019**, 4, 1900337; f) Y. L. Chen, Y. Zhang, T. T. Zhan, Z. M. Lin, S. L. Zhang, H. Y. Zou, G. B. Zhang, C. W. Zou, Z. L. Wang, *Adv. Mater. Technol.* **2019**, 4, 7.  
 [11] Y. Xie, S. Wang, L. Lin, Q. Jing, Z.-H. Lin, S. Niu, Z. Wu, Z. L. Wang, *ACS Nano* **2013**, 7, 7119.  
 [12] B. B. Zhang, J. Chen, L. Jin, W. L. Deng, L. Zhang, H. T. Zhang, M. H. Zhu, W. Q. Yang, Z. L. Wang, *ACS Nano* **2016**, 10, 6241.  
 [13] J. Y. Wang, W. B. Ding, L. Pan, C. S. Wu, H. Yu, L. J. Yang, R. J. Liao, Z. L. Wang, *ACS Nano* **2018**, 12, 3954.  
 [14] G. Zhu, J. Chen, T. J. Zhang, Q. S. Jing, Z. L. Wang, *Nat. Commun.* **2014**, 5, 9.  
 [15] H. Y. Guo, Z. Wen, Y. L. Zi, M. H. Yeh, J. Wang, L. P. Zhu, C. G. Hu, Z. L. Wang, *Adv. Energy Mater.* **2016**, 6, 7.  
 [16] Y. Xi, H. Y. Guo, Y. L. Zi, X. G. Li, J. Wang, J. N. Deng, S. M. Li, C. G. Hu, X. Cao, Z. L. Wang, *Adv. Energy Mater.* **2017**, 7, 1602397.  
 [17] a) C. Zhang, W. Tang, C. Han, F. Fan, Z. L. Wang, *Adv. Mater.* **2014**, 26, 3580; b) Z. Wen, H. Guo, Y. Zi, M.-H. Yeh, X. Wang, J. Deng, J. Wang, S. Li, C. Hu, L. Zhu, Z. L. Wang, *ACS Nano* **2016**, 10, 6526; c) X. Wang, Z. Wen, H. Guo, C. Wu, X. He, L. Lin, X. Cao, Z. L. Wang, *ACS Nano* **2016**, 10, 11369; d) H. Shao, P. Cheng, R. Chen, L. Xie, N. Sun, Q. Shen, X. Chen, Q. Zhu, Y. Zhang, Y. Liu, Z. Wen, X. Sun, *Nano-Micro Lett.* **2018**, 10, 54.

- [18] a) H. J. Shin, J. Y. Choi, S. M. Jang, K. Y. Lim, *IEEE Trans. Magn.* **2013**, 49, 3985; b) G.-H. Jang, M.-M. Koo, J.-M. Kim, J.-Y. Choi, *AIP Adv.* **2017**, 7, 056647.
- [19] J. G. Qian, X. J. Jing, *Nano Energy* **2018**, 52, 78.
- [20] M. T. Rahman, M. Salauddin, P. Maharjan, M. S. Rasel, H. Cho, J. Y. Park, *Nano Energy* **2019**, 57, 256.
- [21] P. H. Wang, L. Pan, J. Y. Wang, M. Y. Xu, G. Z. Dai, H. Y. Zou, K. Dong, Z. L. Wang, *ACS Nano* **2018**, 12, 9433.
- [22] H. Y. Zou, Y. Zhang, L. T. Guo, P. H. Wang, X. He, G. Z. Dai, H. W. Zheng, C. Y. Chen, A. C. Wang, C. Xu, Z. L. Wang, *Nat. Commun.* **2019**, 10, 9.
- [23] M. Xu, Y.-C. Wang, S. L. Zhang, W. Ding, J. Cheng, X. He, P. Zhang, Z. Wang, X. Pan, Z. L. Wang, *Extreme Mech. Lett.* **2017**, 15, 122.
- [24] a) P. H. Wang, R. Y. Liu, W. B. Ding, P. Zhang, L. Pan, G. Z. Dai, H. Y. Zou, K. Dong, C. Xu, Z. L. Wang, *Adv. Funct. Mater.* **2018**, 28, 9; b) Y. L. Zi, H. Y. Guo, Z. Wen, M. H. Yeh, C. G. Hu, Z. L. Wang, *ACS Nano* **2016**, 10, 4797.
- [25] J. S. Alrowaijeh, M. R. Hajj, *Appl. Phys. Lett.* **2018**, 113, 033902.
- [26] D. Kim, I. W. Tcho, Y. K. Choi, *Nano Energy* **2018**, 52, 256.